

# Coupled gas flow-plasma model for a gliding arc: investigations of the back-breakdown phenomenon and its effect on the gliding arc characteristics

SR Sun<sup>1,2</sup>, St Kolev<sup>2,3</sup>, HX Wang<sup>1</sup> and A Bogaerts<sup>2</sup>

<sup>1</sup> School of Astronautics, Beihang University, 100191, Beijing, China

<sup>2</sup> Research group PLASMANT, Department of Chemistry, University of Antwerp, Universiteitsplein 1, B-2610 Antwerp, Belgium

<sup>3</sup> Faculty of Physics, Sofia University, 5 James Bourchier Boulevard, 1164 Sofia, Bulgaria

E-mail: [annemie.bogaerts@uantwerpen.be](mailto:annemie.bogaerts@uantwerpen.be)

**Abstract.** We present a 3D and 2D Cartesian quasi-neutral plasma model for a low current argon gliding arc discharge, including the strong interactions between gas flow and arc plasma column. The 3D model is applied only for a short time of 0.2 ms, due to its huge computational cost. It mainly serves to verify the reliability of the 2D model. As the results in 2D compare well with those in 3D, they can be used for a better understanding of the gliding arc basic characteristics. More specifically, we investigate the back-breakdown phenomenon, induced by an artificially controlled plasma channel, and we discuss its effect on the gliding arc characteristics. The back-breakdown phenomenon, or backward-jump motion of the arc, as observed in experiments, results in a drop of the gas temperature, as well as in a delay of the arc velocity with respect to the gas flow velocity, allowing more gas to pass through the arc, and thus increasing the efficiency of the gliding arc for gas treatment applications.

*Keywords:* gliding arc, quasi-neutral model, back-breakdown phenomenon, 2D model, 3D model

## 1. Introduction

A gliding arc is a non-stationary discharge, usually operating at atmospheric pressure and generating a non-equilibrium plasma, which is gaining interest for high efficiency chemical applications. The periodic arc discharge slides between two divergent electrodes in a gas flow at atmospheric pressure [1-3]. For most prospective plasma chemical applications, the gliding arc has the advantages of simultaneously achieving a high level of non-equilibrium, high electron temperature and high electron density, at a relatively low cost [2]. Therefore, the gliding arc can be used in a wide variety of industrial applications, for example surface treatment [4, 5], waste water degradation using a gliding arc in gas-liquid two phase flow [6], and decomposition of CH<sub>4</sub> into hydrogen [7, 8, 9]. In recent years, there is also growing interest in the conversion of CO<sub>2</sub> into valuable compounds by means of a gliding arc, showing a higher energy efficiency than other non-thermal plasma methods [10-12].

The behavior of the gliding arc discharge is mainly determined by the interactions of the high temperature plasma column with the cold gas flow. The plasma column glides under the influence of a gas flow, and as a result of the increasing electrode distance, the voltage of the plasma column increases together with its length. When the arc voltage is large enough to cause a breakdown between two close parts of the tails of the plasma column, a backward-jump type motion of the arc is produced, which is called the back-breakdown phenomenon. The back-breakdown phenomenon, which reduces the plasma string length, results in a different velocity between arc and gas flow.

There is a growing number of papers on experimental investigations of the so-called back-breakdown phenomenon. Both re-ignitions and back-breakdown events at different gas flow rates have been

investigated experimentally in air [13]. Furthermore, in [14] the time-resolved dynamic behavior of a He and Ar gliding arc plasma was measured with a high-speed camera, and reconnections of the plasma path, i.e., back-breakdown events, were also observed. In [15] the back-breakdown phenomenon was also experimentally investigated, in which the anode and cathode spots remained fixed at the electrodes.

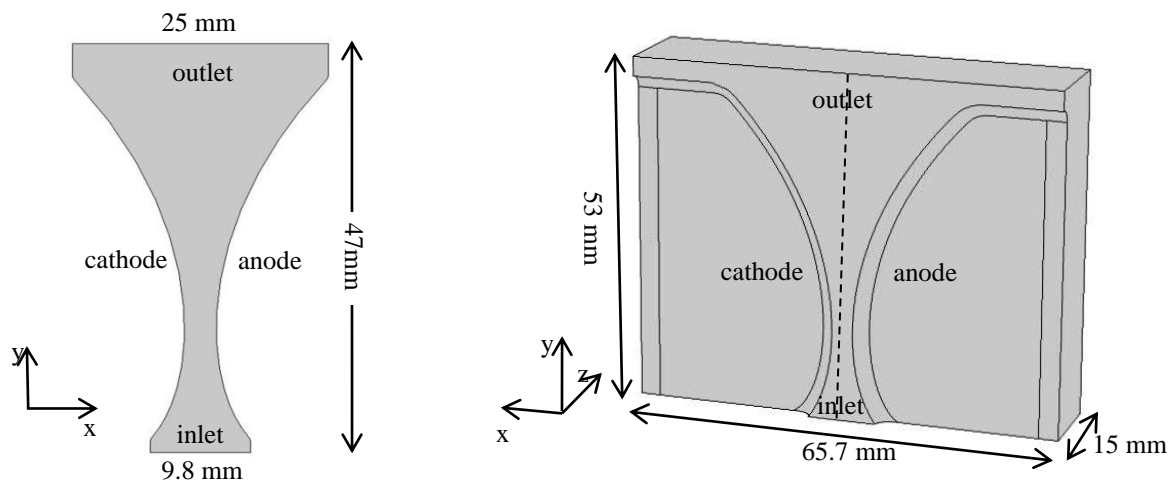
Although several experiments have been performed to study the back-breakdown phenomenon, so far there are no computational models to describe this behavior. A simple analytical model or the simplified Elenbaas-Heller equation have been used to study the basic discharge parameters in previous modeling papers [16-19]. In [20] a comprehensive non-quasi-neutral model of a gliding arc, considering the interactions between arc plasma column and the electrodes, was presented to study the arc root movement. These papers did not present the occurrence of the back-breakdown phenomenon, and the effects of the back-breakdown phenomenon on the plasma characteristics were also not studied. In the present paper, we study both the occurrence of the back-breakdown phenomenon, as well as its influence on the basic plasma characteristics of the gliding arc, more specifically the gas temperature and the electron density, by means of a coupled gas flow-plasma model.

In principle, a gliding arc needs to be modeled in 3D, due to its inherent 3D geometry. However, it is not very realistic to compute a complete arc cycle in a 3D model because of the large number of mesh elements and thus the prohibitively long computation time. On the other hand, some specific aspects, like the arc column size, require a 3D model, to consider the geometry closer to reality. Therefore, in this paper we apply a 3D model for a short time of 0.2 ms, and subsequently we compare the results with the results of a 2D model. This comparison allows to judge the validity of the 2D approach for a realistic description of the gliding arc plasma characteristics.

In the following section, we present the model, and explain the quasi-neutrality assumption and the reduced chemistry set. These approximations are necessary in order to run a 3D model within a reasonable computation time. Subsequently, the results will be presented and discussed. We start with a comparison between the 2D and 3D models, to verify the validity of the 2D model. Next, the occurrence of the back-breakdown phenomenon, and its influence on the gliding arc characteristics, as obtained with a 2D model, will be discussed in detail. Finally, the conclusions on this study will be given.

## 2. Description of the model

### 2.1 The gliding arc geometries



(a) (b)

**Figure 1.** Geometries considered in the model: (a) 2D Cartesian geometry and (b) 3D Cartesian geometry.

The geometries used in the 2D and 3D models are presented in figure 1. The cathode and anode curvature are the same in both geometries. The shortest interelectrode distance is 3.2 mm in both models, which is the same as in the experiment [21]. The 3D geometry shown in figure 1(b) is a cross section through the middle of the anode and the cathode, i.e., the cathode and anode in reality have a width of 4 mm, but only half of it is considered here. The total width of the model geometry, including the region outside the electrodes where the gas can flow without passing through the arc, is 15 mm. In addition, in the calculations another symmetry plane is assumed between the anode and cathode in the 3D model, indicated by the thin dashed line in figure 1(b). This allows us to model 1/4 of the total domain. The latter significantly reduces the calculation time.

## 2.2 The gas discharge and gas flow equations

The model calculates the plasma density, electron and gas temperature, electric field and gas flow behavior in the gliding arc. We assume electrical neutrality in the plasma because the sheath has no significant influence on the arc column. The equations used here for the description of the gliding arc are presented below.

Assuming the drift-diffusion approximation, the species density equation is as follows:

$$\frac{\partial n_s}{\partial t} + \vec{\nabla} \cdot \vec{G}_s + (\vec{u}_g \cdot \vec{\nabla}) n_s = S_{c,s} \quad (1)$$

The species flux  $G_s$  for the ions with respect to the gas is written as follows:

$$\vec{G}_s = \frac{q_s}{|q_s|} \mu_s n_s \vec{E}_{amb} - D_s \vec{\nabla} n_s \quad (2)$$

The ambipolar electric field  $\vec{E}_{amb}$  is derived considering two types of ions ( $\text{Ar}^+$ ,  $\text{Ar}_2^+$ ):

$$\vec{E}_{amb} = \frac{(D_{\text{Ar}^+} - D_e) \vec{\nabla} n_{\text{Ar}^+} + (D_{\text{Ar}_2^+} - D_e) \vec{\nabla} n_{\text{Ar}_2^+}}{(\mu_{\text{Ar}^+} + \mu_e) n_{\text{Ar}^+} + (\mu_{\text{Ar}_2^+} + \mu_e) n_{\text{Ar}_2^+}} \quad (3)$$

The flux  $G_s$  for the neutral species with respect to the gas (in our case the excited atoms  $\text{Ar}(4s)$ ; see below) is as follows:

$$\vec{G}_s = -D_s \vec{\nabla} n_s \quad (4)$$

In these equations,  $n_s$  is the species density,  $u_g$  is the gas velocity (see below) and  $S_{c,s}$  is the collision term representing the net number of particles produced or lost in the volume reactions.  $q_s$  is the charge of the given species type.  $D_s$  is the diffusion coefficient and  $\mu_s$  is the mobility of the corresponding species  $s$ . These diffusion coefficients and mobilities are obtained from [20]. The chemical reactions are presented in section 2.3, and  $S_{c,s}$  is derived from these chemical reactions.

The electron energy equation is solved for the average electron energy density  $n_e \bar{\epsilon}_e$ :

$$\frac{\partial n_e \bar{\varepsilon}_e}{\partial t} + \vec{\nabla} \cdot \vec{G}_{\varepsilon,e} + (\vec{u}_g \cdot \vec{\nabla}) n_e \bar{\varepsilon}_e = \sigma \bar{E}^2 + n_e \Delta \bar{\varepsilon}_e + Q_{bg} \quad (5)$$

Where  $\bar{\varepsilon}_e$  is the averaged electron energy. The plasma electric conductivity is defined as:

$$\sigma = e(\mu_{Ar^+} n_{Ar^+} + \mu_{Ar_2^+} n_{Ar_2^+} + \mu_e n_e) \quad (6)$$

The first term in the right hand side of equation 5 represents the Joule heating term, the second term is the total electron elastic and inelastic collision energy loss term, and the last term  $Q_{bg}$  is the background power density, which is included in order to make the calculations more stable. This background power density yields a background electron density about four orders lower than the arc electron density, so it does not change the arc characteristics. A similar approach of using a background density was also used by others in order to avoid model complications in the context of streamer propagation [22, 23]. The electron energy flux with respect to the gas is expressed as follows:

$$\vec{G}_{\varepsilon,e} = -D_{\varepsilon,e} \vec{\nabla} (n_e \bar{\varepsilon}_e) - \mu_{\varepsilon,e} n_e \bar{\varepsilon}_e \vec{E}_{amb} \quad (7)$$

The electron energy mobility is written as:

$$\mu_{\varepsilon,e} = \frac{5}{3} \mu_e \quad (8)$$

The electron energy diffusion coefficient is [24]:

$$D_{\varepsilon,e} = \frac{2}{3} \mu_{\varepsilon,e} \bar{\varepsilon}_e \quad (9)$$

The electric field is obtained from the current conservation equation:

$$\vec{\nabla} \cdot (-\sigma \vec{\nabla} \phi) = 0 \quad (10)$$

where the electric conductivity  $\sigma$  is given in equation (6), and the electric field is  $\vec{E} = -\vec{\nabla} \phi$ . Note that this electric field is used only for the Joule heating calculation in equation (5) and it does not contribute to the transport of particles and energy.

The gas heat transfer equation is solved for the gas temperature  $T_g$ :

$$\rho C_p \frac{\partial T_g}{\partial t} + \rho C_p \vec{u}_g \cdot \vec{\nabla} T_g - \vec{\nabla} \cdot (k_g \vec{\nabla} T_g) = Q_g \quad (11)$$

where the gas density is  $\rho = m_{Ar} (n_{Ar} + n_{Ar(4s)} + n_{Ar^+} + 2n_{Ar_2^+}) + n_e m_e$ . The heat capacity  $C_p$  at constant pressure and the thermal conductivity  $k_g$  are taken in the form of look-up tables as a function of gas temperature [25].  $Q_g$  is a heat source accounting for energy transfer from the electrons to the heavy particles due to elastic and inelastic collisions. In summary, the system of equations solved for the description of the plasma consists of equations (1), (5), (10) and (11).

The gas flow behavior is described by Navier-Stokes equations, which are solved for a Newtonian fluid :

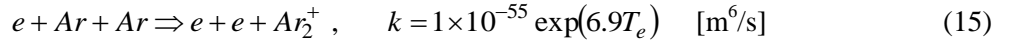
$$\frac{\partial \rho}{\partial t} + \bar{\nabla} \cdot (\rho \bar{u}_g) = 0 \quad (12)$$

$$\rho \frac{\partial \bar{u}_g}{\partial t} + \rho (\bar{u}_g \cdot \bar{\nabla}) \bar{u}_g = \bar{\nabla} \cdot (-p_g \hat{I} + \mu_g (\bar{\nabla} \bar{u}_g + (\bar{\nabla} \bar{u}_g)^T)) - \frac{2}{3} \mu_g (\bar{\nabla} \cdot \bar{u}_g) \hat{I} \quad (13)$$

where  $p_g$  is the pressure, taken as the sum of the partial pressures of all species,  $\mu_g$  is the gas viscosity.  $\hat{I}$  is the identity matrix and the superscript ‘T’ stands for the tensor transpose operation. The inertial term at the left hand side in equation (13) is not included in the 2D model, i.e. in the regime of Stokes flow. In our case, the Navier-Stokes equations are first solved separately in order to provide solutions for a fully developed gas flow, which is subsequently used as initial condition of the system of equations solved in time, which include both the gas and the plasma description.

### 2.3 Chemical reactions and boundary conditions

In order to save computation time, especially for the 3D model, we reduced the number of argon species and chemical reactions from our full argon reaction set described in [20]. Only five important species (instead of seven), i.e., Ar, Ar(4s), Ar<sup>+</sup>, Ar<sub>2</sub><sup>+</sup> and  $e$ , are considered in this paper, and their chemical reactions are the same as the corresponding reactions for these five species in [20]. In order to make sure that the two sets of chemical reactions produce almost the same discharge characteristics, two effective chemical reactions are added in the present model, to replace the contributions of Ar(4p) and Ar<sub>2</sub><sup>\*</sup>. These two effective chemical reactions are as follows:



Eq. (14) is used to replace the stepwise ionization process due to Ar(4p), while equation (15) replaces the process  $e + Ar_2^* \Rightarrow e + e + Ar_2^+$ , which is considered as the main contributor to the ionization due to Ar<sub>2</sub><sup>\*</sup>. The two reaction rate coefficients are obtained by fitting the corresponding rates to the main chemical reaction rates of Ar(4p) and Ar<sub>2</sub><sup>\*</sup> in [20]. We assume that the two rate coefficients are only a function of temperature. This approximation works well in our conditions, but it is not necessarily applicable to other discharge conditions. This reduced reaction set keeps the important species and chemical reactions, and it can produce almost the same plasma characteristics as in [20] at a reduced calculation time, so it is also suitable for the 3D model. The specific chemical reactions and corresponding reaction rate coefficients adopted in the present model are given in table 1. The rate coefficients for the electron reactions and the electron mobility are calculated with a Boltzmann solver ‘‘BOLSIG+’’ [24].

The boundary conditions to solve the above equations are defined as follows. For the species density and electron energy equations, zero species flux and zero electron energy flux are set at walls, and zero gradient of the species density and the electron energy density are set at the inlet and the outlet. The thermal insulation boundary condition is used on the electrode walls; the temperature is fixed at 293.15 K at the inlet, while a zero temperature gradient is assumed at the outlet. For the gas flow description, the normal inflow velocity is defined at the inlet, and the pressure is set to 101 kPa at the outlet. The gas flow follows no slip boundary condition on the electrode walls. The anode electric potential is connected to ground. The cathode potential is derived from Ohm’s law based on the total cathode current and external circuit. The specific expressions of these boundary conditions for the 2D

model are given in table 2. The boundary conditions for the 3D model are the same as those in the 2D model except for the inlet velocity condition. A Gaussian profile of the inlet velocity with velocity magnitude 25 m/s and standard deviation distance 1.5 mm is used in the 3D model. So the expression is as follows:

$$u_g = 25 \exp\left(-\left(\frac{x^2}{2(1.5 \times 10^{-3})^2}\right) - \left(\frac{z^2}{2(1.5 \times 10^{-3})^2}\right)\right) \quad [\text{m/s}] \quad (16)$$

**Table 1.** Chemical reactions used in the model and corresponding reaction rate coefficients

Reaction	Rate coefficient
$e+\text{Ar} \rightarrow e+\text{Ar}$	BS <sup>a</sup>
$e+\text{Ar} \rightarrow e+\text{Ar}(4s)$	BS
$e+\text{Ar} \rightarrow 2e+\text{Ar}^+$	BS
$e+\text{Ar}(4s) \rightarrow 2e+\text{Ar}^+$	BS
$e+\text{Ar}(4s) \rightarrow e+\text{Ar}$	BS, DB <sup>b</sup>
$2e+\text{Ar}^+ \rightarrow e+\text{Ar}$	$k(\text{m}^6/\text{s}) = 8.75 \times 10^{-39} T_e^{-2.25} (\text{eV})$
$e+\text{Ar}+\text{Ar}^+ \rightarrow \text{Ar}+\text{Ar}$	$k(\text{m}^6/\text{s}) = 1.5 \times 10^{-40} (T_g(\text{K})/300)^{-2.5}$
$e+\text{Ar}_2^+ \rightarrow \text{Ar}+\text{Ar}^+ + e$	$k(\text{m}^3/\text{s}) = 1.11 \times 10^{-12} \exp(-(2.94 - 3(T_g(\text{eV}) - 0.026))/T_e(\text{eV}))$
$e+\text{Ar}_2^+ \rightarrow \text{Ar}(4s)+\text{Ar}$	$k(\text{m}^3/\text{s}) = 1.04 \times 10^{-12} \left(\frac{300}{T_e(\text{K})}\right)^{0.67} \frac{1 - \exp(-418/T_g(\text{K}))}{1 - 0.31 \exp(-418/T_g(\text{K}))}$
$\text{Ar}(4s)+\text{Ar}(4s) \rightarrow e+\text{Ar}_2^+$	$k(\text{m}^3/\text{s}) = 3.15 \times 10^{-16} (T_g(\text{K})/300)^{-0.5}$
$\text{Ar}(4s)+\text{Ar}(4s) \rightarrow e+\text{Ar}^+ + \text{Ar}$	$k(\text{m}^3/\text{s}) = 1.62 \times 10^{-16} (T_g(\text{K}))^{0.5}$
$2\text{Ar}+\text{Ar}^+ \rightarrow \text{Ar}_2^+ + \text{Ar}$	$k(\text{m}^6/\text{s}) = 2.5 \times 10^{-43} \left(\frac{T_g(\text{K})}{300}\right)^{-1.5}$
$\text{Ar}_2^+ + \text{Ar} \rightarrow 2\text{Ar}+\text{Ar}^+$	$k(\text{m}^3/\text{s}) = \frac{6.06 \times 10^{-12}}{T_g(\text{K})} \exp\left(-\frac{1.51 \times 10^4}{T_g(\text{K})}\right)$
$\text{Ar}(4s) \rightarrow h\nu + \text{Ar}$	$\nu_c(\text{s}^{-1}) = g_{eff}^c \times 3.145 \times 10^8$
$e+\text{Ar} \rightarrow e+e+\text{Ar}^+$	$k(\text{m}^3/\text{s}) = 2 \times 10^{-33} \exp(10.2 T_e(\text{eV}))$
$e+\text{Ar}+\text{Ar} \rightarrow e+e+\text{Ar}_2^+$	$k(\text{m}^6/\text{s}) = 1 \times 10^{-55} \exp(6.9 T_e(\text{eV}))$

a. Boltzmann solver

b. Detailed balance

c.  $g_{eff} = (1.15/\pi)(\lambda_{4s}/(6H))$ , where  $\lambda_{4s} = 105.7$  nm and  $H = 1$  mm in our case.

**Table 2.** Boundary conditions used in the 2D model; see the text for the equation numbers.  $V_c$  is the cathode potential with respect to the grounded anode.

Equations	(1)	(5)	(10)	(11)	(13)
inlet	$\vec{n} \cdot \vec{\nabla} n_s = 0$	$\vec{n} \cdot \vec{\nabla} n_e \vec{\mathcal{E}}_e = 0$	$\vec{n} \cdot \vec{\nabla} \phi = 0$	$T_g = 293.15$ K	$\vec{n} \cdot \vec{u}_g = 5$ ms <sup>-1</sup>
outlet	$\vec{n} \cdot \vec{\nabla} n_s = 0$	$\vec{n} \cdot \vec{\nabla} n_e \vec{\mathcal{E}}_e = 0$	$\vec{n} \cdot \vec{\nabla} \phi = 0$	$\vec{n} \cdot \vec{\nabla} T_g = 0$	$p = 101$ kPa
cathode	$\vec{n} \cdot \vec{G}_s = 0$	$\vec{n} \cdot \vec{G}_{\mathcal{E},e} = 0$	$\phi = V_c$	$\vec{n} \cdot \vec{\nabla} T_g = 0$	$u_g = 0$
anode	$\vec{n} \cdot \vec{G}_s = 0$	$\vec{n} \cdot \vec{G}_{\mathcal{E},e} = 0$	$\phi = 0$	$\vec{n} \cdot \vec{\nabla} T_g = 0$	$u_g = 0$

### 3. Results and discussions

### 3.1 Comparison between 2D and 3D models

As mentioned above, the gliding arc discharge geometry makes the model description inherently a 3D problem, more specifically for the description of the arc diameter. In literature, the number of real 3D plasma models is very limited, and most 3D models are based on local thermodynamic equilibrium [26-30] or on the two-temperature thermal non-equilibrium and chemical equilibrium assumption [31]. In our paper the 3D model is calculated without these simplifications, but at the expense of the computational cost. The aim of this section is to compare the performance of the 2D and 3D models and to determine the validity of the 2D approach.

Two assumptions are used in the comparison between the 2D and 3D models. The first one is that the gas velocity at the shortest interelectrode distance is the same in both models. In the 2D model, Stokes flow is used in order to avoid instabilities caused by the dimensionality, while in the 3D model, laminar flow is adopted. The validity of this laminar flow assumption can be assessed by the Reynolds number. In case of a gas temperature of 300 K, the argon density ( $\rho$ ) is  $1.78 \text{ kg m}^{-3}$ , the gas velocity ( $u_g$ ) at the shortest interelectrode distance in the 3D model ( $d = 3.2 \text{ mm}$ ) is  $22 \text{ m/s}$ , and the argon viscosity ( $\mu_g$ ) is  $3.67 \times 10^{-5} \text{ kg m}^{-1} \text{ s}^{-1}$ , so the resulting Reynolds number ( $\text{Re} = \rho u_g d / \mu_g$ ) is about 3400. However, taking into account the increase of gas temperature, the gas density will decrease, while the viscosity will increase, so the Reynolds number will decrease. For example, in case of a gas temperature of 1000 K, the gas density is  $0.52 \text{ kg m}^{-3}$ , the gas viscosity is  $6.9 \times 10^{-5} \text{ kg m}^{-1} \text{ s}^{-1}$ , so the Reynolds number is about 600. Taking into account that in a pipe flow [32], a laminar flow corresponds to  $\text{Re} < 2300$ ,  $2300 < \text{Re} < 4000$  stands for a transition flow, and  $\text{Re} > 4000$  represents a turbulent flow, we can conclude that our assumption of a laminar flow as used in the 3D model is reasonable.

The second assumption is that the electrical current is the same, in order to compare the 2D and 3D results at the same calculation conditions. In the 2D model, the simulated geometry is considered to be infinite in the direction perpendicular to the simulation plane, i.e., the arc is not a “wire” but a “slab”, so the current in the 2D model is obtained by assuming that the current density in the “z” direction has the same distribution as along the “y” axis, i.e., as if it is a cylindrical “wire”. Thus the current in the 2D model is obtained by line integration of the current density over the arc region on the y axis ( $x=0$ ,  $I = \int \sigma E 2\pi r dr$ ). In 3D model, however, the arc shape is self-consistently obtained to be very close to a cylindrical wire, and the actual arc diameter can be automatically calculated. So the total arc current in the 3D model is obtained by surface integration of the current density over a cross section in the yz plane.

With these two assumptions, the calculation conditions are defined as follows. In the 3D model, the gas flow rate is 10 l/min with inlet velocity profile given by equation (16), the voltage source is 3700 V, and the resistance is 120 k $\Omega$ . In the 2D model, the gas flow rate cannot be specified, because no inlet area can be specified in 2D, but the normal inflow velocity is set to 5 m/s, in order to obtain the same gas velocity distribution at the shortest interelectrode distance as in the 3D model (cf. above). The voltage source is also 3700 V, but the resistance is set to 66  $\Omega \text{ m}^{-1}$  in order to obtain the same current as in the 3D model. Special attention is also paid to the mesh element size, which is the same for both models. The maximum element size is 100  $\mu\text{m}$  in the area where the arc body passes. Using this mesh element size, the 3D model has in total 680 000 mesh elements and takes about three days to calculate over a time of 0.2 ms. Moreover, in the 3D model, these small mesh elements are only applied in the arc area, and not in the whole domain. Therefore, the large computational cost of the 3D simulations makes it impractical to study the long-term behavior of the gliding arc. For this reason, we

want to compare the results between the 2D and 3D models within this limited time-scale of 0.2 ms. If there are no significant differences, we may conclude that the 2D model is capable of providing useful qualitative and quantitative information on the discharge behavior.

The gas temperature profiles in the symmetry plane ( $xy; z=0$ ), calculated with the 2D and 3D models, are presented in figure 2, at the same time of 0.2 ms. It can be seen that the absolute value of the gas temperature in the 2D and 3D models is almost the same. The maximum gas temperature at the symmetry axis (the position marked with an arrow in figure 2) is about 1163 K in the 3D model, while it is about 1151 K in the 2D model.

The comparison of the electron density between the 2D and 3D models is presented in figure 3, again in the symmetry plane ( $xy; z=0$ ) and at the time of 0.2 ms. The difference in electron densities at the arrow marked position is about 30%, which is somewhat larger than the difference between the gas temperatures. Indeed, the electron density in the 3D model (with maximum value of  $3.6 \times 10^{20} \text{ m}^{-3}$  at the arrow marked position) is slightly higher than in the 2D model (i.e.,  $2.4 \times 10^{20} \text{ m}^{-3}$ ). Also the shape and the electron density values before and after the arc are slightly different.

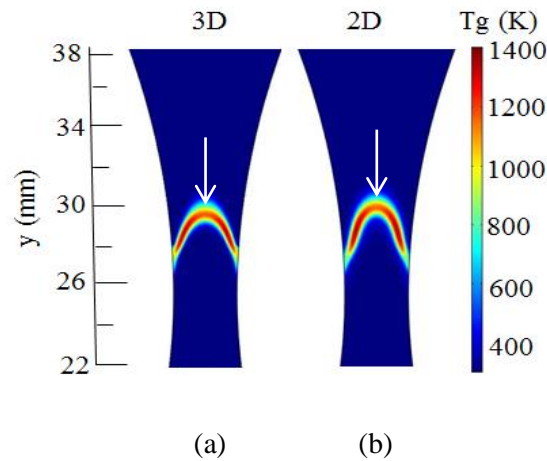


**Figure 2.** Calculated gas temperature distributions in the symmetry plane ( $xy; z=0$ ), at a time of 0.2 ms, as obtained with the 3D model (a) and 2D model (b).

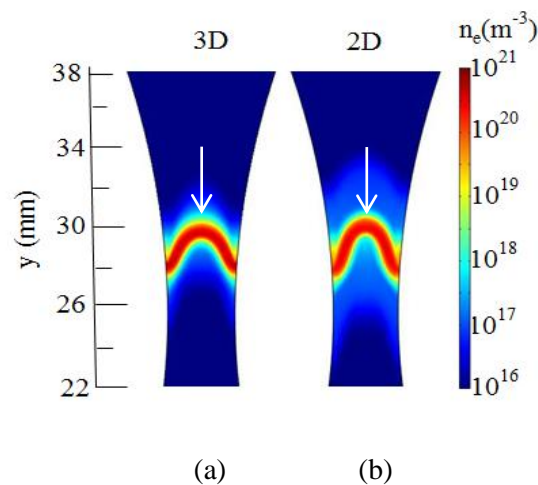


**Figure 3.** Calculated electron density distributions in the symmetry plane ( $xy; z=0$ ), at a time of 0.2 ms, as obtained with the 3D model (a) and 2D model (b).

In general we can conclude that, although the arc shape in the 2D model (i.e., a “slab” instead of a “wire”) is inherently different from the real arc shape, as represented in the 3D model, a good agreement between the 2D and 3D models can be reached by adjusting these two models to have the same calculation conditions. Besides the gas temperature and electron density, other plasma characteristics have also been compared, such as the ion densities and the electron temperature. The difference in the electron density is non-negligible, but it is still within the acceptable range. The difference between the ion densities was the same as for the electron density. The slight difference in electron density is caused by the production rate due to chemical reactions, which is slightly larger in the 3D model. The resulting difference in the gas temperature is very small, because the gas temperature is subjected to the same cooling due to the arc extension, as well as the same heating due to elastic collisions between electrons and heavy particles. Although the maximum electron density in the arc core is slightly different, the total electron density integrated over the plasma column is almost the same. This is probably because of the stronger contraction in the 3D model due to additional conductive cooling in the ‘z’ direction, which is missing in the 2D model and which causes a stronger inhomogeneity in the 3D model. The difference in electron temperature is similar to the difference in gas temperature, i.e., the maximum electron temperature at the arrow marked position in figure 2 is 2.56 eV for the 3D model and 2.50 eV for the 2D model. So we can conclude that the 2D approach is reasonable and useful to investigate the gliding arc behavior, within an acceptable calculation time. This will be illustrated in the next sections.

### ***3.2 Occurrence of the back-breakdown phenomenon***

As mentioned in the Introduction, some experiments [13, 15] report on the so-called back-breakdown phenomenon as a breakdown between both tails of the arc, which can occur as a result of the arc bending due to the gas flow, providing a shorter path to the arc current compared to the previous current path. This breakdown appears upstream (i.e., close to the arc-electrode contacts) and thus it can be considered as a backward jump-like motion of part of the arc. This back-breakdown phenomenon is responsible for the different velocity between arc and gas flow, and this velocity difference between cold gas and arc can make sure that more gas can pass through the arc when travelling through the reactor, and can thus be treated (e.g., converted) in a real gliding arc reactor. However, the back-breakdown event is mostly stochastic by nature and it is not well defined. If we want to describe it directly in our model, we need to consider the arc-gas instabilities, and produce a similar irregular plasma string as in experiments. However, a fluid plasma model cannot describe such behavior, and Monte Carlo models should be employed to study this in detail.

To circumvent this problem, and to be able to produce the back-breakdown phenomenon in our fluid model, an artificial plasma channel, i.e. an artificial heating term, which is space and time dependent, is added to equation (5) above. The artificial plasma channel can be triggered on a regular or irregular basis with respect to the arc path or time, i.e., every certain distance or period, a back-breakdown can be initiated. Both algorithms (i.e., distance or time) are similar. We employ the following algorithm for a distance controlled back-breakdown:

1. We define the distance between consecutive back-breakdown events;
2. The “trajectory” of the arc is obtained according to the gas velocity distribution, so we can define a time dependent function which is the sum of several Gaussian functions, each one being displaced in time and centered at the time of the back-breakdown events.
3. We find the positions of maximum electron density at the electrodes ( $(x1, y1)$  and  $(-x1, y1)$ ) and at the symmetry axis ( $x=0, y2$ ). These numbers approximately determine the current position of the arc.
4. We use these numbers ( $x1, y1, y2$ ) to define the position of the back-breakdown event, i.e. to define the spatial function of the back-breakdown addition to the heating term. More specifically, the  $y$

position of the back-breakdown event is defined as  $y_{bb}=y1+(y2-y1)*r_y$ , assuming  $r_y=0.4$ . The  $x$  position of the back-breakdown event is  $x_{bb}=r_x*(y_{bb}-y2)*x1/(y1-y2)$ , assuming  $r_x=0.7$ . The formulas are deduced from the shape of the region surrounded by the arc, which is considered as a triangle. The quantities  $r_x$  and  $r_y$  are external setting parameters. The value of  $r_y$  is chosen in order to provide a reduction of the arc in  $y$  direction. The  $r_x$  is chosen in a way that the artificial channel connects exactly both tails of the arc for the given  $r_y$ . Note that in reality  $r_x$  and  $r_y$  could be different for the different back-breakdown events.

5. After obtaining the time and space distribution functions of the heating term, this heating term for producing the back-breakdown is added to equation (5). The minimum heat source used for producing the back-breakdown is  $10^{10}$  W/m<sup>3</sup>, and thus the expression with only one time function term is as follows:

$$10^{10} \exp\left(-\frac{(y_{bb}-y)^2}{2(1.5 \times 10^{-4})^2}\right) \times \exp\left(-\frac{(x)^4}{2(x_{bb})^4}\right) \times \exp\left(-\frac{(t-3 \times 10^{-4})^2}{2(6 \times 10^{-6})^2}\right) \quad [\text{W/m}^3] \quad (17)$$

In case of a time-controlled back-breakdown, the time can be directly determined instead of steps 1 + 2. From step 3, the algorithms are the same for both distance and time controlled back-breakdown.

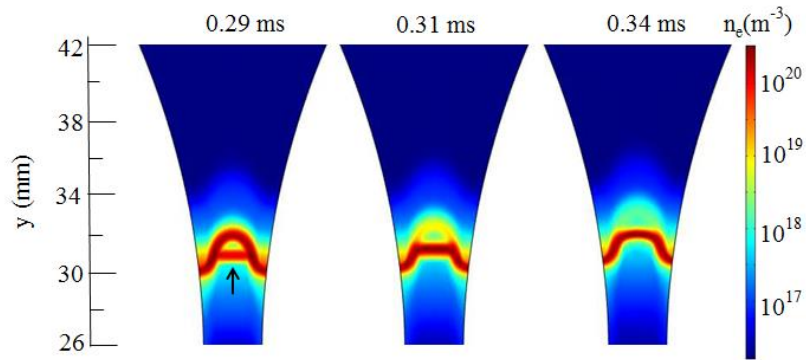
Figure 4 presents the time-evolution of the electron density distribution, illustrating a single back-breakdown process, at an arc current of 30.8 A/m, a voltage source  $V=3700$  V, with  $R=120$  Ω/m. The figure shows that an artificial, high electron density area in the order of  $10^{19}$ - $10^{20}$  m<sup>-3</sup> (i.e., about half the maximum electron density in the arc) is added just below the arc (indicated by an arrow at time 0.29 ms in figure 4). Because this new channel provides a shorter electric current path and a lower resistance, the new arc is established here (figure 4,  $t=0.34$  ms) and thus the back-breakdown occurs.

Figure 5 presents the periodic occurrence of several back-breakdown events, occurring each time after a travelled distance of about 3 mm. Initiating the back-breakdown events based on a regular distance instead of based on time is probably more favorable, because physically, the arc length and thus the arc voltage drop is connected with the arc movement along the curved electrodes. Note that a higher arc voltage drop increases the probability of back-breakdown events, although as noted before, the gas-arc instabilities can also facilitate the back-breakdown appearance.

The arc voltage variation as a function of time during these successive back-breakdown events is plotted in figure 6. The evolution of the arc voltage during the initial ignition process is also shown, and is plotted as an inset in figure 6 in order to clearly see the trend. After the peak voltage reaches 300 V, it is followed by an immediate sharp drop to 200 V during a very short time of 0.01 ms. This is because at the beginning, the gas electrical conductivity is very low, so when adding the artificial heating term to initiate the discharge, the gas resistance decreases in a short time, thus leading to a sharp voltage drop. Then the voltage drops further to 100 V in about 0.1 ms, because a stable plasma channel is formed, i.e., the discharge is ignited at the shortest interelectrode distance. Subsequently, the voltage slightly rises again under the influence of the gas flow, but at about 0.3 ms, 0.6 ms and 1 ms, marked with circles, sharp drops in the voltage are observed, which are correlated to the occurrence of the back-breakdown events illustrated in figure 5. Indeed, the sharp voltage drop during the back-breakdown process is due to the increase of the electron temperature and the creation of an artificial plasma channel when triggering the added artificial heating source, and the corresponding increase of electric conductivity. The reason is that during the back-breakdown process, two channels exist in parallel for a short time and this significantly reduces the total arc resistance, which indeed causes a sharp voltage drop. This drop is followed each time by a sharp increase of the voltage, due to the drop in electron temperature and the added plasma channel when the artificial heating source stops,

and also the decay of the older channel. Finally, when a shorter current path is built after the back-breakdown event, the voltage first slightly decreases, and then begins to increase again under the influence of the gas flow. Therefore, the arc voltage fluctuations take place together with the back-breakdown phenomena. This is similar to the voltage waveform in several experiments. Indeed, the experiments also exhibit sharp arc voltage fluctuations when some back-breakdown events are occurring [13, 15, 33].

Although we use an artificial heating term to produce the back-breakdown events in our model, the same backward-jump motion of the arc as in experiments can be produced, and the fluctuations of the arc voltage are also similar to the experimental voltage waveforms when back-breakdown events occur. Therefore, we can use our model to investigate the effect of the back-breakdown events on the gliding arc characteristics, as will be explained in the next section.



**Figure 4.** Time-evolution of the electron density distribution, illustrating a single back-breakdown event, at an arc current of 30.8 A/m, a voltage source  $V=3700$  V, with  $R=120$   $\Omega/m$ .

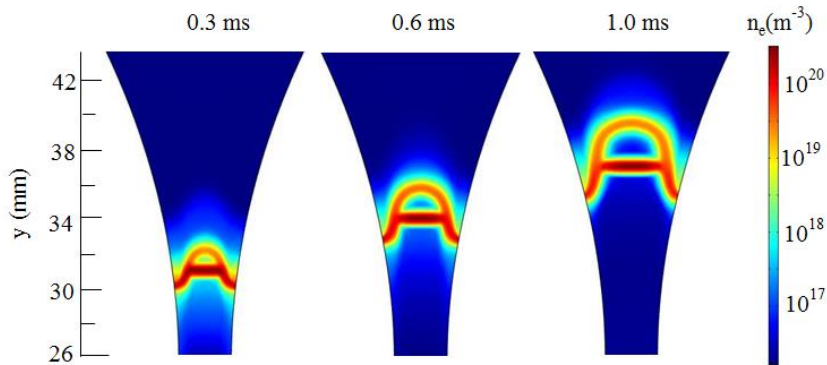


**Figure 5.** Time-evolution of the electron density distribution, illustrating consecutive back-breakdown events, at an arc current of 30.8 A/m, a voltage source  $V=3700$  V, with  $R=120$   $\Omega/m$ .

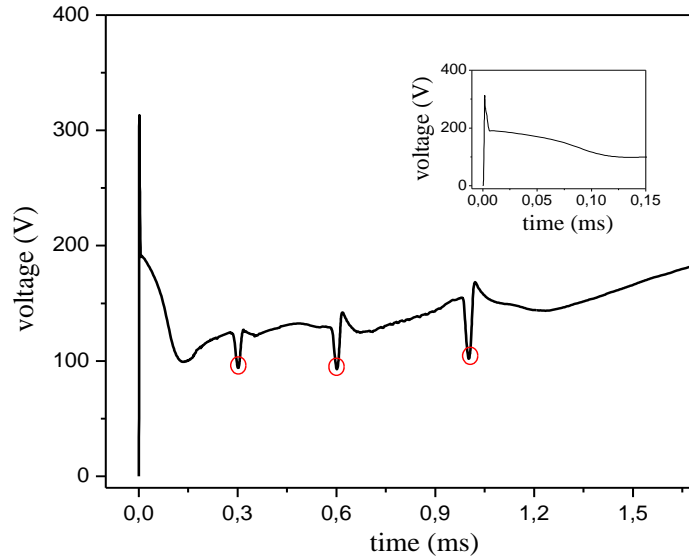


**Figure 6.** Time evolution of the arc voltage during three consecutive back-breakdown events, for the same calculation conditions as in figure 5.

### 3.3 Influence of the back-breakdown phenomenon on the gliding arc characteristics

It is known that the arc velocity will show a delay with respect to the gas flow velocity after occurrence of a back-breakdown event. However, the question arises whether, in addition to this effect, the back-breakdown events also affect the plasma properties in another way. From figures 4 and 5, the answer seems no, because the absolute value of the electron density does not obviously change after the back-breakdown event, only the position of the electron density changes. However, from the time-evolution of the gas temperature, plotted in figure 7(a), we can clearly see the influence of the back-breakdown event on the gas temperature. In order to better clarify this effect, the time-evolution of the gas temperature without back-breakdown is also plotted in figure 7(b). From these two figures, we can see that the gas temperature in both cases is the same before the back-breakdown occurs (time 0.3 ms), but after the back-breakdown event, the gas temperature in figure 7(a) is obviously lower than in figure 7(b), especially at the center between both electrodes, i.e., the symmetry axis ( $x=0$ ). In figure 7(a), the gas temperature at this position is about 700 K and 890 K at time 0.4 ms and 0.5 ms, respectively, while in figure 7(b), the gas temperature at the same position, and again at time 0.4 ms and 0.5 ms, is about 900 K and 1000 K, respectively. So we can conclude that the back-breakdown event is an efficient mechanism for gas cooling, because the heat is spread over a larger domain and not only within the initial arc channel. This is basically a pulsed-like operation of the discharge and every new back-breakdown forces the arc to move to the cold gas region. Thus the gas is subject to heating for only a short time, due to the back-breakdown event. In this way, an old, somewhat cooler plasma column appears above the newly formed thermal plasma column, as illustrated in figure 7(a), while there is always only one hot plasma column in figure 7(b). Furthermore, figure 7(a) also clearly indicates the delay in arc velocity compared to the case without back-breakdown event (i.e., figure 7(b)).

Figure 8 illustrates the effect of two different back-breakdown frequencies on the gas temperature profile along the  $y$ -axis at the symmetry axis ( $x=0$ ). The position of  $y=0$  is set at the shortest interelectrode distance, and the data points are obtained within a time frame of 1 ms, at a frequency of 0.1 ms, starting from 0.1ms, so there are 10 data points in total for each case. When there is no back-breakdown, the gas temperature keeps rising with the  $y$  position (black curve). When a back-breakdown is induced with a time interval of 0.3 ms (red curve), the first back-breakdown starts at 0.3

ms, followed by another one at 0.6 ms and a last one at 0.9 ms (hence three back-breakdown events in total within the time range of 1 ms). Thus at the beginning, the gas temperature is the same as in the case without back-breakdown, but then it drops three times, corresponding to the three back-breakdown events. When a back-breakdown is induced every 0.1 ms (blue curve), we also let the first back-breakdown event occur at 0.3 ms, but in total it occurs seven times within the time range of 1 ms. In this case, the gas temperature is clearly lower and only fluctuates within a very small range. This is because the gas does not have enough time to be heated due to the frequent back-breakdown events. Therefore, the back-breakdown phenomenon obviously reduces the gas temperature, and the more frequently the back-breakdown events occur, the larger will be the drop in gas temperature.

Finally, besides the drop in gas temperature and the delay in arc velocity with respect to the gas velocity, we expect that the back-breakdown event will also lead to more efficient gas treatment in a gliding arc discharge, because it can produce a so-called sweeping effect of the gas to be treated. Indeed, the sweeping effect is due to the different velocities between arc and cold gas, i.e., a portion of the gas enters the arc column region, and after being treated (e.g., converted to another component) within the arc, it leaves the arc region due to its larger velocity. Subsequently, a new portion of cold gas enters the arc body and is also treated, and this process repeats itself. In this way, a larger fraction of the gas can be treated (or converted) in a gliding arc discharge.

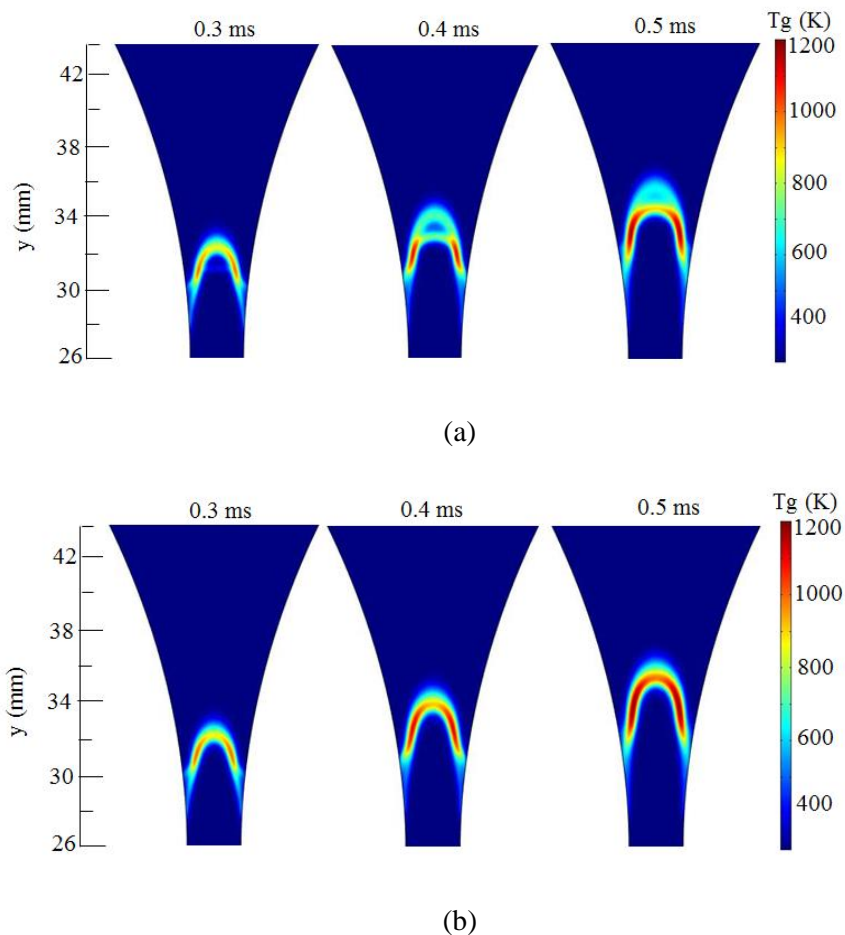


**Figure 7.** Time evolution of the gas temperature at an arc current of 30.8 A/m, a voltage source  $V=3700$  V, with  $R=120$   $\Omega/m$ , for two different cases, i.e., with back-breakdown (a) and without back-breakdown (b).

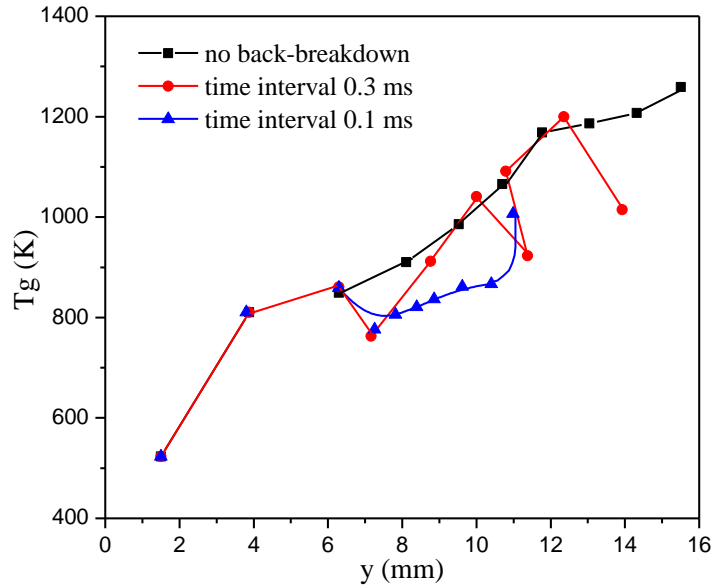


**Figure 8.** Influence of the back-breakdown frequency on the gas temperature profile along the y-axis, for the same calculation conditions as in figure 7. Position  $y=0$  corresponds to the shortest interelectrode distance.

#### 4. Conclusions

In this paper, we present a fully coupled gas flow-plasma quasi-neutral model for a low current argon gliding arc plasma, both in 2D and 3D. This model allows for a detailed self-consistent description of the interactions between gas flow, heat transfer and plasma reaction kinetics. The interaction of the cold gas flow with the high temperature plasma column is indeed important for studying the gliding arc characteristics. In the present model, a laminar flow model is employed due to the small gas velocity. However, our next step is to couple a complex turbulent flow with the plasma discharge model, considering the turbulence dissipation heat loss, so that the model will also be valid for larger gas velocities.

In principle, a 3D model would be required to describe the gliding arc behavior in a realistic way, in view of the intrinsic 3D nature of the gliding arc. However, a 3D model is very time consuming, and could therefore only be calculated for a short time, to keep the calculation time reasonable. In order to check the validity of a 2D model for describing the gliding arc characteristics, the results of the 3D model are compared with 2D model results under the same calculation conditions. The difference in plasma characteristics is small, especially for the gas and electron temperature, justifying the use of a 2D model to investigate the gliding arc behavior within a reasonable calculation time.

The 2D model is then used to investigate the back-breakdown phenomenon, by applying an artificially controlled plasma channel. The same backward jump-like motion of the arc as in experiments could be produced, and the calculated arc voltage fluctuations are also similar to the experimental waveforms when back-breakdown events are occurring. The back-breakdown events cause a delay in the arc velocity compared to the gas flow velocity. Moreover, they have a great influence on the gas temperature, leading to a significant drop in the gas temperature, because the heat is now spread over a larger domain and not only within the initial arc channel. Finally, when the gliding arc is used for gas treatment (e.g., gas conversion), the back-breakdown event can also produce a so-called sweeping effect of the gas to be treated, due to the different velocity between arc and gas flow, and thus increase the efficiency of the gliding arc reactor for gas treatment applications.

## Acknowledgment

This work is financially supported by the Methusalem financing, by the Fund for Scientific Research Flanders (FWO) and by the IAP/7 (Inter-university Attraction Pole) program "Physical Chemistry of Plasma-Surface Interactions" from the Belgian Federal Office for Science Policy (BELSPO). The work was carried out in part using the Turing HPC infrastructure of the CalcUA core facility of the Universiteit Antwerpen, a division of the Flemish Supercomputer Center VSC, funded by the Hercules Foundation, the Flemish Government (department EWI) and the Universiteit Antwerpen. This work was also supported by the National Natural Science Foundation of China. (Grant Nos. 11275021, 11072020).

## References

- [1] Czernichowski A, 1994 Gliding arc. Applications to engineering and environment control *Pure & Appl. Chem.*, 66(6): 1301-1310
- [2] Fridman A, Nester S, Kennedy L A, Saveliev A and Mutaf-Yardimci O, 1999 Gliding arc gas discharge *Progress in energy and combustion science* 25: 211-231
- [3] Richard F, Cormier J M, Pellerin S and Chapelle J, 1997 Gliding arcs fluctuations and arc root displacement *High Temp. Material Processes* 1: 239-248
- [4] Kusano Y, Norrman K, Drews J et al., 2011 Gliding arc surface treatment of glass-fiber-reinforced polyester enhanced by ultrasonic irradiation *Surface & Coatings Technology* 205: S490-S494
- [5] Kusano Y, Sorensen B F, Andersen T L and Leipold F 2013 Adhesion Improvement of glass-fibre-reinforced polyester composites by gliding arc discharge treatment *J. Adhes.* 89 433-59
- [6] Tu X, Yu L, Yan J H, Cen K F and Cheron B G, 2009 Dynamic and spectroscopic characteristics of atmospheric gliding arc in gas-liquid two-phase flow *Physics of Plasma* 16: 113506-1-5
- [7] Lee H, Sekiguchi H 2011 Plasma-catalytic hybrid system using spouted bed with a gliding arc discharge: CH<sub>4</sub> reforming as a model reaction *J. Phys. D: Appl. Phys.* 44: 274008 (8pp)
- [8] Kalra C S, Gutsol A F and Fridman A A 2005 Gliding arc discharges as a source of intermediate plasma for methane partial oxidation *IEEE Trans. Plasma Sci.* 33 32-41
- [9] Tu X, Whitehead J C, 2014 Plasma dry reforming of methane in an atmospheric pressure AC gliding arc discharge: Cogeneration of syngas and carbon nanomaterials *International Journal of Hydrogen Energy* 39: 9658-9669
- [10] Indarto A, Choi J W, Lee H and Song H K, 2006, Conversion of CO<sub>2</sub> by Gliding Arc Plasma *Environmental Engineering Science* 23(6): 1033-1043
- [11] Indarto A, Yang D R, Choi J W, Lee H and Song H K, 2007 Gliding arc plasma processing of CO<sub>2</sub> conversion *Journal of Hazardous Materials* 146: 309-315
- [12] Kim S C, Lim M S and Chum Y N, 2014 Reduction Characteristics of Carbon Dioxide Using a Plasmatron *Plasma Chem Plasma Process* 34: 125-143
- [13] Zhu J, Sun Z, Li Z, Ehn A, Alden M, Salewski M, Leipold F and Kusano Y 2014 Dynamics, OH distributions and UV emission of a gliding arc at various flow-rates investigated by optical measurements *J. Phys. D: Appl. Phys.* 47 295203 (11pp)
- [14] Mitsugi F, Furukawa J, Ohshima T, Kawasaki H, Kawasaki T, Aoqui S and Stryczewska H D 2013 Observation of dynamic behavior of gliding arc discharge *Eur. Phys. J.: Appl. Phys.* 61: 24308-1-4
- [15] Pellerin S, Martinie O, Cormier J M, Chapelle J and Lefauchaux P 1999 Back-breakdown phenomenon in low current discharge at atmospheric pressure in transversal flow *High Temp. Mater. Process.* 2 167-80
- [16] Kuznetsova I V, Kalashnikov N Y, Gutsol A F, Fridman A A and Kennedy L A 2002 Effect of 'overshooting' in the transitional regimes of the low-current gliding arc discharge *J. Appl. Phys.* 92 4231-7

- [17] Richard F, Cormier J M, Pellerin S and Chapelle J 1996 Physical study of a gliding arc discharge *J. Appl. Phys.* 79 2245–50
- [18] Pellerin S, Richard F, Chapelle J, Cormier J-M and Musiol K 2000 Heat string model of bi-dimensional dc Glidarc *J. Phys. D: Appl. Phys.* 33 2407–19
- [19] Pellerin S, Cormier J-M, Richard F, Musiol K and Chapelle J 1999 Determination of the electrical parameters of a bi-dimensional dc glidarc *J. Phys. D: Appl. Phys.* 32 891–7
- [20] Kolev St and Bogaerts A 2015 A 2D model for a gliding arc discharge *Plasma Sources Sci. Technol.* 24 015025
- [21] Tu X, Gallon H J, Whitehead J C 2011 Electrical and optical diagnostics of atmospheric pressure argon gliding arc plasma jet *30th ICPIG (Belfast, UK, 28 August– 2 September, 2011)* C10
- [22] Boeuf J-P, Yang L L and Pitchford L C 2013 Dynamics of a guided streamer ('plasma bullet') in a helium jet in air at atmospheric pressure *J. Phys. D: Appl. Phys.* 46: 015201
- [23] Wormeester G, Pancheshnyi S, Luque A, Nijdam S and Ebert U 2010 Probing photo-ionization: simulations of positive streamers in varying N<sub>2</sub>:O<sub>2</sub>-mixtures *J. Phys. D: Appl. Phys.* 43: 505201
- [24] Hagelaar G J M and Pitchford L C 2005 Solving the Boltzmann equation to obtain electron transport coefficients and rate coefficients for fluid models *Plasma Sources Sci. Technol.* 14: 722-733
- [25] Murphy A B, Arundell C J 1994 Transport Coefficients of Argon, Nitrogen, Oxygen, Argon-Nitrogen, and Argon-Oxygen Plasmas *Plasma Chemistry and Plasma Processing* 14: 451-490
- [26] Freton P, Gonzalez J J and Gleizes A 2000 Comparison between a two- and a three-dimensional arc plasma configuration *J. Phys. D: Appl. Phys.* 33: 2442–2452
- [27] Gonzalez J J, Lago F, Freton P, Masquere M and Franceries X 2005 Numerical modeling of an electric arc and its interaction with the anode: part II. The three-dimensional model—influence of external forces on the arc column *J. Phys. D: Appl. Phys.* 38: 306–318
- [28] Gonzalez J J, Freton P and Gleizes A 2002 Comparisons between two- and three-dimensional models: gas injection and arc attachment *J. Phys. D: Appl. Phys.* 35: 3181–3191
- [29] Trelles J P, Pfender E, Heberlein J V R 2006 Multiscale Finite Element Modeling of Arc Dynamics in a DC Plasma Torch *Plasma Chem Plasma Process* 26: 557–575
- [30] Trelles J P, Pfender E and Heberlein J V R 2007 Modelling of the arc reattachment process in plasma torches *J. Phys. D: Appl. Phys.* 40: 5635–5648
- [31] Trelles J P, Heberlein J V R and Pfender E 2007 Non-equilibrium modelling of arc plasma torches *J. Phys. D: Appl. Phys.* 40 5937–5952
- [32] Holman J P 2002 Heat Transfer *McGraw-Hill*. p. 207.
- [33] Delair L, Brisset J L and Cheron B G 2001 Spectral electrical and dynamical analysis of a 50Hz air gliding arc *High Temp. Mater. Process.* 5 381–403